From typhoon rainfall to slope failure: optimizing susceptibility models and dynamic thresholds for landslide warnings in Zixing City, China

Weifeng Xiao[1], Guangchong Yao[1], Zhenghui Xiao[1], Ge Liu[*2], Luguang Luo[1], Yunjiang Cao[1], Wei Yin[3]

[1]School of Earth Sciences and Spatial Information Engineering, Hunan University of Science and Technology, Xiangtan 411201, China

[2]Northeast Institute of Geography and Agroecology, CAS, Changchun 130102, China

[3]Hunan Institute of Geological Disaster Investigation and Monitoring, Changsha 410004, China

Corresponding author.

E-mail address: liuge@iga.ac.cn (Ge Liu)

Abstract: Typhoon-specific rainfall-induced landslides pose critical hazards in mountainous regions, yet existing warning systems inadequately capture the distinct rainfall dynamics of these extreme events. To address this limitation, we propose an integrated framework combining optimized susceptibility predictions with dynamic rainfall thresholds tailored to typhoon patterns. The approach enhances machine learning accuracy through buffer-based negative sampling and variable weighting. It also introduces a spatiotemporal rainfall analysis to distinguish between short-term intense downpours and cumulative soil saturation. Tested in Zixing City, Hunan Province, China, where over 700 landslides were triggered by Typhoon Gaemi, the framework proved effective. The support vector machine (SVM) model achieved the best performance using frequency ratio (FR) inputs with a 0.5 km buffer (F1-score: 0.859, AUC: 0.914), correctly classifying 86.4% of landslides as high or very high susceptibility. The rainfall analysis identified 24-hour intensity combined with 7-day antecedent rainfall as the optimal trigger, effectively capturing both immediate and cumulative moisture effects. Spatially, rhyolite and granite slopes and areas near roads emerged as hotspots for failure

28 (distance < 800 m, FR = 1.499 for roads; FR = 1.546 for rhyolite). The integrated warning

29 system shows high spatial efficiency, with high-risk areas covering only 34.2% of the study

30 region yet capturing 71.4% of historical landslides. Additionally, the framework generated

31 high-risk zone maps that align strongly with historical events. This work highlights the unique

32 nature of typhoon-driven slope instability and provides a transferable framework for disaster

33 risk reduction in cyclone-prone regions.

34 **Keywords:** Typhoon-induced landslide; Slope failure; Hazard warning system; Dynamic

35 thresholds; Landslide susceptibility mapping

36 **1 Introduction**

37 Landslides pose significant threats to mountainous regions globally (Froude and Petley,

38 2018), especially in areas where steep terrain, complex geology (Thiene et al., 2017), and

39 extreme weather events like typhoons intersect. In Southeast China, typhoon-induced

40 landslides have become a growing concern due to the region's rapid urbanization and the

41 increasing variability in climate patterns (Gariano and Guzzetti, 2016; Fan et al., 2018). The

42 Nanling Mountains, in southern China, are particularly vulnerable to landslides due to a

43 combination of extreme topographic relief and complex geological conditions during the

44 typhoon season (Zou et al., 2023).

45 Typhoons typically bring prolonged antecedent rainfall, followed by intense, short bursts

46 of precipitation (Li et al., 2019). These conditions create unique hydrological environments

47 that exceed the complexity of typical rainfall-triggered landslides (Chung and Li, 2022).

48 These events trigger slope failures through cumulative soil saturation and sudden hydrological

49 stress, challenging traditional landslide prediction methods (Yang et al., 2017). Despite

50 advances in landslide susceptibility prediction (LSP) and rainfall threshold modeling, current

51 approaches remain inadequate. Three critical limitations persist: severe data imbalance effects,

52 suboptimal integration of variable selection with machine learning algorithms, and lack of

spatially-explicit rainfall thresholds for typhoon-specific conditions (Segoni et al., 2018a; Regmi et al., 2024).

Most existing studies employ ad-hoc buffer distances without systematic optimization, leading to inconsistent model performance across different geological settings (Lombardo and Mai, 2018). Traditional methods attempt to mitigate this imbalance by randomly sampling non-landslide points across the study area (Steger et al., 2016; Dou et al., 2023). However, random selection can introduce spatial bias, as non-landslide points might include areas that are unstable but have not yet been identified as landslide-prone (Kalantar et al., 2018).

To address this limitation, more recent approaches have employed buffer-based negative sampling, which systematically excludes non-landslide points near known landslide sites. This method assumes that adjacent areas share similar environmental conditions (e.g., slope, lithology) and therefore should not be classified as "stable" (Achu et al., 2022). Several studies have tested varying buffer distances, ranging from tens to thousands of meters, to determine the optimal distance for different regions. However, systematic evaluation of buffer distance optimization coupled with variable weighting methods remains largely unexplored.

LSP is primarily focused on identifying areas prone to slope failure, based on static environmental factors such as topography, lithology, land cover, and hydrology (Zêzere et al., 2017; Guo et al., 2024). Traditional approaches to LSP often rely on deterministic and statistical methods, including information value (IV), certainty factor (CF), frequency ratio (FR), logistic regression (LR), and weight of evidence (WOE). These methods quantify the relationship between historical landslide occurrences and predisposing factors using linear or semi-linear approaches (Ciurleo et al., 2017; Reichenbach et al., 2018). However, these methods oversimplify the complex, nonlinear interactions that govern slope stability (Merghadi et al., 2020).

In contrast, machine learning (ML) algorithms, such as support vector machine (SVM) and light gradient boosting machine (LightGBM), have emerged as powerful alternatives. SVM excels in high-dimensional classification tasks and effectively identifies optimal hyperplanes separating landslide-prone from stable areas (San, 2014; Huang and Zhao, 2018). LightGBM offers superior scalability and computational efficiency for processing large geospatial datasets (Sun et al., 2023). Both SVM and LightGBM capture intricate relationships among variables without restrictive assumptions, making them superior to traditional methods in terms of predictive accuracy (Yang et al., 2023). However, frameworks that systematically integrate variable weighting methods with advanced ML algorithms for LSP optimization are lacking.

For temporal prediction, existing rainfall threshold approaches predominantly use generalized regional thresholds that inadequately capture local geological heterogeneity and typhoon-specific rainfall patterns (Guzzetti, 2021; Banfi and De Michele, 2024). These thresholds are typically defined based on cumulative or intensity-duration (I-D) rainfall values (Piciullo et al., 2017; Segoni et al., 2018a). In typhoon-prone regions, dynamic rainfall thresholds are crucial due to the unique combination of long-duration antecedent rainfall and sudden high-intensity bursts of precipitation (Guzzetti et al., 2020). Traditional empirical methods fail to provide spatially continuous threshold surfaces that account for local environmental variability (Piciullo et al., 2018).

Recent advances have integrated multi-temporal rainfall parameters with advanced statistical techniques to optimize rainfall thresholds (Segoni et al., 2015; Huang et al., 2022), accounting for diverse triggering mechanisms. Additionally, spatial interpolation methods, such as Kriging, have been applied to generate continuous rainfall threshold surfaces that allow for local variations in geological and environmental conditions (Kenanoglu et al., 2019; Segoni et al., 2018b). This approach, when combined with high-resolution susceptibility maps,

102   contributes to the development of integrated hazard warning systems that can dynamically

103   adjust to typhoon-specific rainfall-induced scenarios (Piciullo et al., 2018; Mirus et al., 2018).

104   This study examines Zixing City, a mountainous region in southeastern Hunan Province,

105   frequently affected by typhoon-induced extreme rainfall. Its steep slopes, fractured geology,

106   and high sensitivity to rapid pore-pressure increase render it particularly vulnerable (Ma et al.,

107   2025). The large number of landslides (>700) triggered by Typhoon Gaemi in July 2024

108   provides a valuable dataset for model calibration and validation.

109   Here we developed an integrated framework that combines (i) optimized buffer distances

110   for negative sampling, (ii) bivariate weighting methods (IV, CF, FR) with advanced machine

111   learning classifiers (SVM, LightGBM), and (iii) spatially continuous, typhoon-specific

112   rainfall thresholds derived through Kriging interpolation. The specific objectives are to (1)

113   determine optimal buffer distances that minimize spatial bias in imbalanced datasets, (2)

114   evaluate the performance gain from coupling bivariate weights with machine learning

115   algorithms, (3) establish dynamic rainfall thresholds suited to typhoon rainfall patterns, (4)

116   generate continuous threshold surfaces via Kriging, and (5) integrate high-resolution

117   susceptibility maps with these thresholds to support an operational early warning system. This

118   approach improves landslide prediction in typhoon-prone mountainous regions and provides a

119   transferable methodology for similar environments.

120 **2   Study area and data sources**

121   **2.1   Study area**

122   Zixing City (25°34′–26°18′ N, 113°08′–113°44′ E), covering 2,747 km² in southeastern

123   Hunan Province, China (Fig. 1), is located within the Nanling Mountains geological province.

124   Situated approximately 400 km inland from the South China Sea, Zixing lies at the

125   intersection of the Nanling Mountains and low hills, forming a watershed divide between the

126   Yangtze and Pearl River basins. The region is characterized by steep topography, with

127 elevations ranging from 125 to 1,691 meters and slopes exceeding 30° across 78% of the area.

128 This mountainous terrain, combined with fractured geology and active NE-SW trending faults

129 such as the Chaling-Yongxing Fault Zone, creates a permeable fracture network that

130 facilitates groundwater drainage.

131   The climate of Zixing is subtropical monsoon, with annual precipitation averaging 1,550

132 mm, 70% of which occurs from April to September. Typhoons significantly contribute to

133 rainfall, inducing rapid pore-pressure increases in shallow aquifers (3–8 m depth). These

134 climatic and geological conditions make Zixing particularly vulnerable to landslides,

135 providing a valuable context for this study. The extensive landslide dataset triggered by

136 Typhoon Gaemi in July 2024 (>700 events) serves as a critical resource for model calibration

137 and validation.
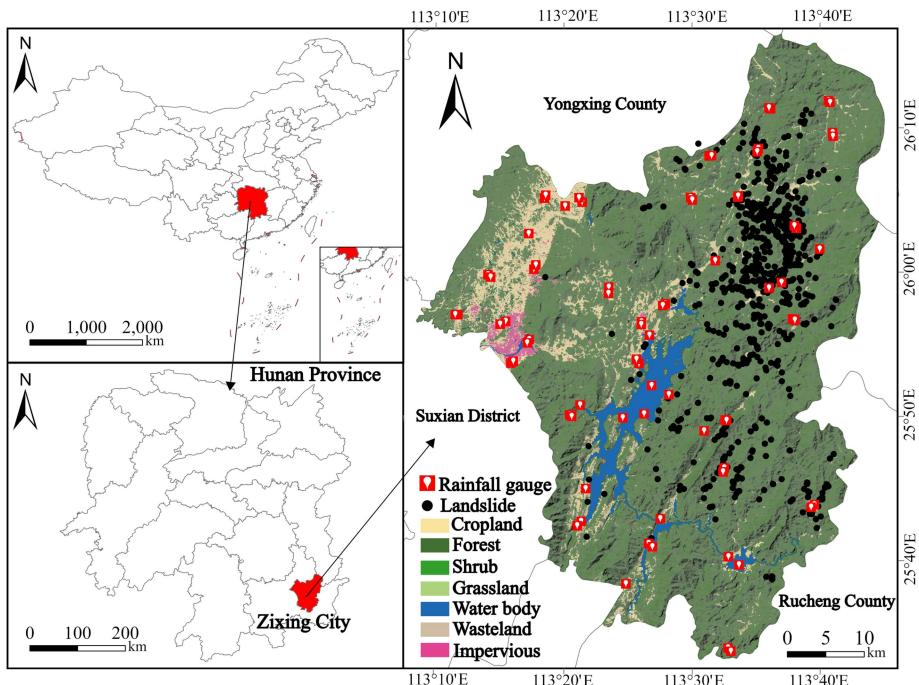
138

139   **Figure 1** Geographical distribution of the study area, landslides and rainfall gauges.

140 **2.2 Data collection and preprocessing**

141 **2.2.1 Compilation of landslide catalogue**

142   A comprehensive inventory of 705 landslide events triggered by Typhoon Gaemi on July

143 27, 2024, was compiled from the Hunan Center for Natural Resources Affairs. The landslide

144 locations were verified through field inspections and high-resolution satellite imagery to

145 ensure spatial accuracy and completeness of the dataset.

2.2.2 Landslide conditioning factors and data sources

147 Based on extensive literature reviews and the geoenvironmental characteristics of the

148 study area, twelve conditioning factors were selected for landslide susceptibility analysis:

149 elevation, slope gradient, slope orientation, curvature, topographic wetness index (TWI),

150 stream power index (SPI), normalized difference vegetation index (NDVI), distances to roads,

151 rivers, and faults, and lithology (Fig. 2).

152 Topographic factors (elevation, slope gradient, slope orientation, TWI, SPI, and

153 curvature) were extracted from a 30-meter digital elevation model (DEM) obtained from the

154 Geospatial Data Cloud (https://www.gscloud.cn). Environmental factors including NDVI and

155 proximity variables (distances to roads, rivers, and fault lines) were derived from 1:50,000-

156 scale cartographic maps and Landsat 8 OLI imagery from the same platform. Geological

157 composition and structural data were acquired from 1:100,000-scale geological maps.

158

159

160

161

162
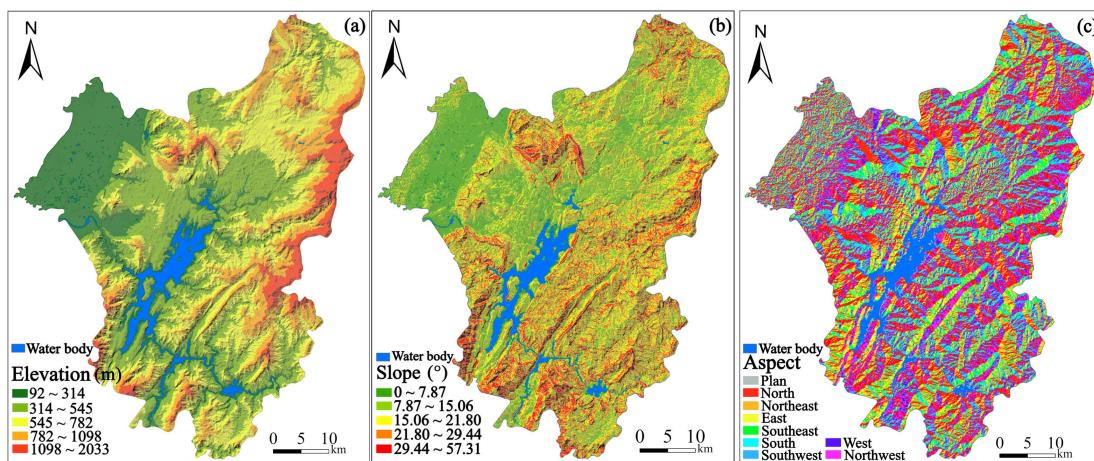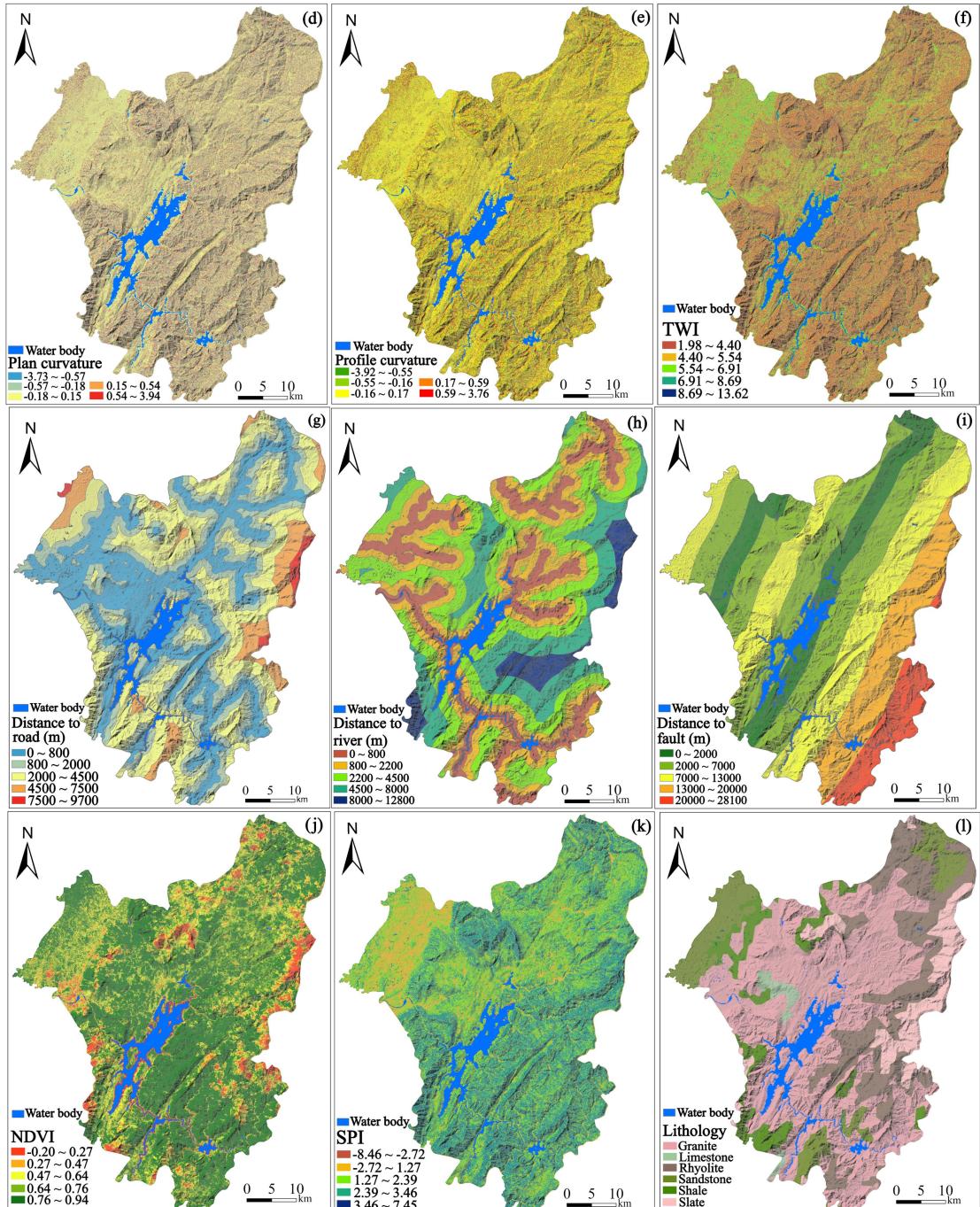
Figure 2 Landslide-related conditioning factors.

2.2.3 Data preprocessing and spatial standardization

163

164 We transformed all conditioning factors into continuous statistical measures using IV,

165 CF, and FR methods and then resampled them to a uniform 60-meter resolution. This

166 resolution was selected to balance computational efficiency with scale appropriateness for

167 regional landslide analysis while maintaining compatibility with the available geological map

168 scale (1:100,000).

169   The study area was divided into 60×60 meter grid cells, with landslides smaller than the

170   grid resolution aggregated to the nearest cell centroid. Multiple landslides within a single cell

171   were treated as one event to maintain spatial independence required for machine learning

172   modeling. This preprocessing approach ensures statistical validity by minimizing spatial

173   autocorrelation effects while providing adequate representation of landslide distribution

174   patterns across the study area.

175   **2.2.4 Rainfall data collection and spatial distribution**

176   Rainfall data for the study were obtained from 12 automatic rain gauge stations

177   strategically distributed across Zixing City and its surrounding areas (Fig. 1). These stations,

178   operated by the Hunan Meteorological Administration, provided hourly precipitation records

179   during Typhoon Gaemi (July 20–30, 2024) and the preceding antecedent period. The spatial

180   distribution of gauge stations ensured adequate coverage of the study area's topographic and

181   climatic gradients.

182   To assign rainfall parameters (H1, H12, H24, H72, and D7) to each of the 705 landslide

183   points, we employed the Kriging interpolation to generate spatially continuous rainfall

184   surfaces from discrete gauge measurements. This geostatistical method accounts for spatial

185   autocorrelation in rainfall patterns and provides optimal unbiased estimates by weighting

186   nearby observations based on their spatial proximity and correlation structure.

187   Spherical variogram models were fitted to the rainfall data through iterative optimization,

188   with model selection based on minimum Akaike Information Criterion (AIC) values. The

189   interpolation accuracy was rigorously evaluated through leave-one-out cross-validation,

190   where each gauge station was sequentially removed and its rainfall values predicted using the

191   remaining 11 stations. Four statistical metrics were used to assess performance: Root Mean

192   Square Error (RMSE), Mean Absolute Error (MAE), correlation coefficient (R), and Nash-

193   Sutcliffe Efficiency (NSE).

194

Table 1 Kriging interpolation accuracy assessment for rainfall parameters.

Parameter	RMSE (mm)	MAE	R	NSE
H1	4.2	3.1	0.76	0.71
H12	11.7	8.9	0.83	0.78
H24	16.3	12.6	0.87	0.82
H72	24.8	18.4	0.81	0.77
D7	29.6	22.7	0.78	0.73

195   The validation results demonstrated acceptable interpolation accuracy across all rainfall

196   parameters, with correlation coefficients ranging from 0.76 to 0.87 and Nash-Sutcliffe

197   Efficiency values between 0.71–0.82. Despite some limitations inherent to the sparse gauge

198   network in mountainous terrain, the interpolation performance was deemed sufficient for

199   regional landslide susceptibility analysis, ensuring reasonable spatial representation of

200   precipitation patterns across the study area.

201   **3   Methodologies**

202   This study proposes an integrated framework for optimizing LSP and typhoon-specific

203   rainfall thresholds within hazard warning systems (Fig. 3). The framework includes the

204   following key components: (1) landslide susceptibility prediction and mapping, utilizing

205   twelve conditioning factors prioritizing typhoon-induced hydrological responses (e.g., TWI,

206   SPI) and 705 landslide records from July 27, 2024, optimized with five buffer distances and

207   evaluated using ROC curves; (2) dynamic rainfall threshold modeling based on typhoon

208   rainfall parameterization, validated and spatially interpolated using Kriging; and (3) the

209   integration of spatial and temporal probabilities to develop a typhoon-specific rainfall-induced

210   landslide warning system, demonstrated through a case study in Zixing City.
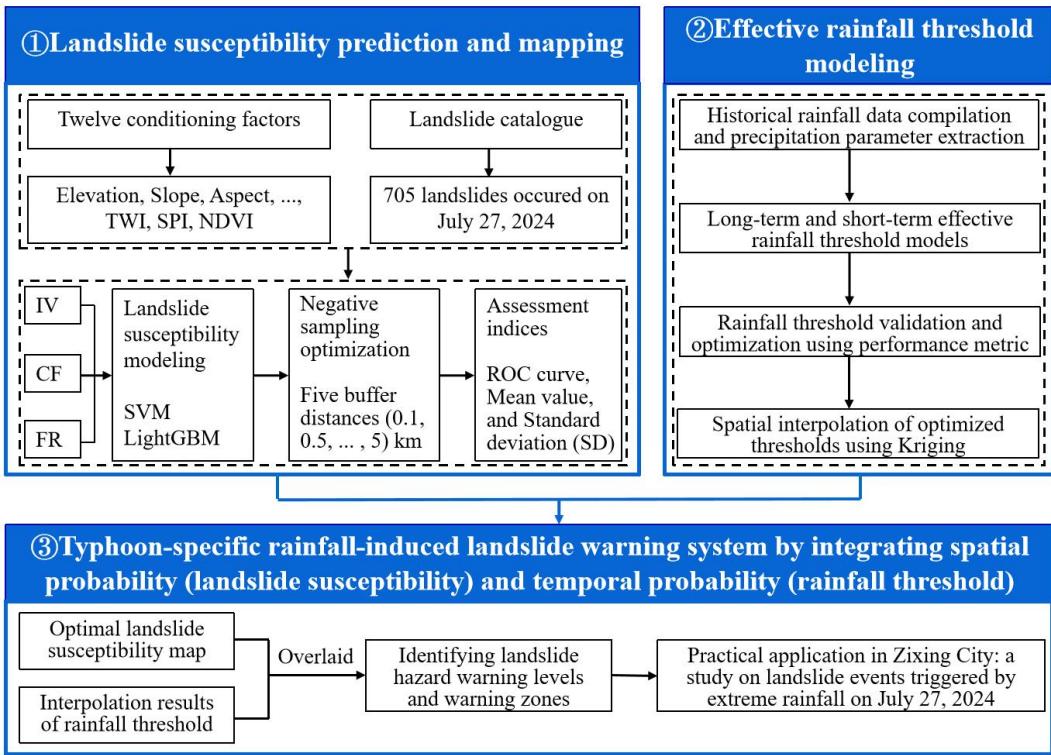
Figure 3 Technical framework for developing a typhoon-specific rainfall-induced landslide warning system.

3.1 Landslide susceptibility prediction and mapping

3.1.1 Machine learning models: selection rationale and implementation

We selected SVM and LightGBM to address three key challenges in typhoon-specific rainfall-induced landslide prediction: (1) severe class imbalance (landslides <0.5% of study area), (2) complex non-linear interactions between rainfall and terrain factors, and (3) computational efficiency for operational early warning.

SVM excels in binary classification with limited samples through structural risk minimization (Kalantar et al., 2018; Wang et al., 2020), making it suitable for typhoon-triggered landslide mapping. Its margin-maximization approach handles the class imbalance between stable and landslide areas, while the RBF kernel captures localized failure patterns under concentrated typhoon rainfall. The regularization parameter C prevents overfitting to specific typhoon events, ensuring model transferability. The SVM optimization problem is defined as:

226
$$\min_{w,b,\xi} \frac{1}{2} w^T w + C \sum_{i=1}^{n} \xi_i \qquad (1)$$

227 subject to the constraint:

228
$$y_i(w^T \phi(x_i) + b) \geq 1 - \xi_i, \quad \xi_i \geq 0, \quad i = 1, \cdots, n \qquad (2)$$

229 where w is the normal vector to the hyperplane, b is the bias term, ξ_i are slack

230 variables, $\phi(x_i)$ maps input vectors to a higher-dimensional space, and y_i denotes the class

231 label (-1 or 1) for each sample x_i. We optimized the RBF kernel parameters using grid-search

232 with 5-fold cross-validation, where $C \in [0.1, 100]$ and $\gamma \in [0.001, 1]$. Across all

233 configurations (three input methods × five buffer distances), optimal values varied as follows:

234 $C = 5–15$ and $\gamma = 0.10–0.25$, with median values of $C = 10$ and $\gamma = 0.15$.

235 LightGBM complements SVM through gradient boosting with sequential error

236 correction, offering distinct advantages for regional-scale landslide mapping. Its histogram-

237 based algorithm enables efficient processing of large spatial datasets (Sun et al., 2023; Sahin,

238 2020). Additionally, LightGBM automatically captures complex feature interactions. The

239 minimized objective function is expressed as:

240
$$L = \sum_{i=1}^{N} (y_i - \hat{y}_i)^2 + \lambda \sum_{j=1}^{M} \left\| \theta_j \right\|^2 \qquad (3)$$

241 where y_i is the true label, $\hat{y}_i$ is the predictive value, λ is a regularization parameter, and

242 θ_j represents the parameters of the model. We optimized LightGBM hyperparameters through

243 Bayesian optimization. The optimal hyperparameters ranged as: num_leaves = 25–35,

244 learning_rate = 0.03–0.08, and max_depth = 6–10. Early stopping with a 50-round patience

245 window resulted in model convergence at 120–220 trees across different scenarios.

246 **3.1.2   Input variable weighting methods**

247 The IV method, grounded in information theory, assesses how different factors

248 contribute to landslide susceptibility within a study area (Niu et al., 2024). Factors such as

distance to roads and lithology were weighted higher in Zixing City due to their interaction with typhoon-induced soil saturation. The IV for each evaluation factor is determined using the formula below:

$$IV(F_i, K) = \ln \frac{N_i / N}{S_i / S} \tag{4}$$

where $IV(F_i, K)$ is the information value of evaluation factor F_i in relation to landslide event K, N_i refers to the number of landslides, N is the total number of landslides, S_i represents the area covered by factor F_i, and S is the total area of the study area.

The CF method is a widely utilized probabilistic technique for assessing the likelihood of landslide occurrences (Zhao et al., 2021). It quantifies the prior probability of a landslide initiation under specific conditions of influential factors, utilizing spatial data from known landslide locations. The expression of CF is as follows:

$$CF = \begin{cases} \dfrac{PP_a - PP_s}{PP_s(1 - PP_a)}, & PP_a < PP_s \\[3mm] \dfrac{PP_a - PP_s}{PP_a(1 - PP_s)}, & PP_a \geq PP_s \end{cases} \tag{5}$$

where CF is the certainty factor indicating the degree of association between an influential factor and potential landslide occurrence. It is derived from two area-proportional measures: PP_a, the proportion of landslide points within a specific factor class (number of landslide points in the class / total area of the class); and PP_s, the proportion of landslide points across the entire study region (total number of landslide points / total area of the region).

The FR is a prevalent method in statistical analysis that assesses the relative impact of various factors on the incidence of landslides (Panchal et al., 2021). An elevated FR value denotes a more significant influence of a factor on the likelihood of landslides. The FR is determined by the following equation:

$$FR = \frac{N_i / N}{S_i / S} \tag{6}$$

271 where *FR* is the frequency ratio, N_i represents the number of landslides within the area

272 corresponding to the conditioning factor, *N* is the total number of landslides, S_i is the area

273 covered by the conditioning factor and *S* is the total area of the study region.

3.1.3 Buffer distance optimization and uncertainty assessment for LSP

275 To generate negative (non-landslide) samples for LSP, areas within buffer distances of d

276 = 0.1, 0.5, 1.0, 2.0, and 5.0 km around landslide locations were excluded, with balanced

277 negative samples (n = 705) randomly selected from remaining stable areas for each distance.

278 The optimal buffer distance was determined by evaluating SVM and LightGBM model

279 performance using AUC, Precision, Recall, and F1-score metrics.

280 The selection of buffer distances (0.1–5.0 km) was based on Zixing's geomorphological

281 considerations and practices commonly reported in LSP. This range encompasses multiple

282 spatial scales: slope-scale processes (0.1–0.5 km), catchment-scale features (1.0–2.0 km), and

283 regional-scale geological units (5.0 km). The evaluation ensures optimal spatial representation

284 without a priori assumptions about scale dependencies (Chang et al., 2023).

285 Prediction uncertainty was assessed using the mean and standard deviation (SD) of

286 predicted landslide susceptibility values. Lower mean and SD values indicate reduced

287 prediction uncertainty and more concentrated susceptibility patterns, suggesting higher model

288 confidence in LSP (Huang et al., 2022), thereby complementing the buffer distance

289 optimization process.

3.2 Effective rainfall threshold modeling

3.2.1 Rainfall parameterization and threshold calculation

292 Typhoon-induced landslides are generally influenced by a combination of antecedent

293 moisture conditions and immediate precipitation, rather than by isolated rainfall events

294 (Mondini et al., 2023; Tufano et al., 2021). To account for the cumulative impact of multi-day

rainfall while incorporating hydrological processes such as evapotranspiration and drainage, we adopted the concept of effective rainfall (P_e), calculated as:

$$P_e = \sum_{i=0}^{n} k^i P_i \qquad (7)$$

where P_i represents the daily rainfall on the i-th day preceding landslide occurrence, n denotes the number of antecedent days considered, and k is the effective rainfall decay coefficient (Segoni et al., 2018a). For hourly rainfall parameterization, P_i is derived as:

$$P_i = \sum_{j=1}^{24} R_{ij} \qquad (8)$$

where R_{ij} is the hourly rainfall at the j-th hour of the i-th day.

3.2.2 Long-term and short-term rainfall parameters

Rainfall-triggered landslides are generally triggered by two dominant mechanisms: prolonged low-intensity rainfall and short-duration high-intensity storms. Based on statistical analysis of historical landslide events in Hunan Province (Xiao et al., 2025), a 7-day antecedent period was identified as optimal for characterizing long-term rainfall impacts. Consequently, the 7-day effective rainfall (D7) was selected as the long-term parameter. Short-term rainfall metrics were defined as cumulative precipitation over 1 hour (H1), 12 hours (H12), 24 hours (H24), and 72 hours (H72) preceding landslide initiation. These intervals capture distinct rainfall characteristics: H1 reflects extreme short-term intensity for rapid slope failures, H12 and H24 represent sub-daily to daily precipitation critical for intermediate responses, and H72 accounts for multi-day storm sequences.

3.2.3 Rainfall threshold model development

The threshold modeling framework comprises three sequential steps:

(1) Parameter calculation: For each landslide sample, short-term rainfall parameters (H1, H12, H24, and H72) and the long-term rainfall parameter (D7) are calculated. The ratios of

318 short-term parameters to the long-term parameter are computed as: R1=H1/D7, R12=H12/D7,

319 R24=H24/D7, and R72=H72/D7.

320 (2) Threshold setting: Long-to-short-term ratio coefficients (RC1, RC12, RC24, and

321 RC72) are introduced as thresholds to determine the dominant rainfall pattern for each

322 landslide. These thresholds are used to classify landslides into short-term or long-term

323 Typhoon-induced categories.

324 (3) Coefficient optimization: A cyclic trial-and-error method is employed to determine

325 the optimal ratio coefficients (RC1, RC12, RC24, and RC72), maximizing the accuracy and

326 reliability of the model.

3.2.4   Optimal ratio coefficient threshold determination

328 The process of determining the optimal long-to-short-term ratio coefficient threshold is

329 demonstrated using H12-D7 as an example. The process for the remaining coefficients (H1-

330 D7, H24-D7, and H72-D7) follows a similar approach. A 5-fold cross-validation method is

331 applied, with the following procedure:

332 (1) Rainfall data extraction for landslide locations: For each of the 705 landslide points,

333 R12 and D7 values are extracted from these interpolated surfaces at the exact landslide

334 coordinates, ensuring that each landslide location receives rainfall values derived from the

335 spatially weighted contributions of all nearby gauge stations. R12 and D7 values for each

336 landslide are calculated using Equations (7) and (8).

337 (2) Data preparation: The dataset is divided into five equal parts for cross-validation,

338 with each part serving as a test set while the remaining four serve as the training set.

339 (3) Initial threshold setting: An initial threshold for RC12 is set based on the minimum

340 value in the training set.

341 (4) Threshold evaluation: For each fold, the RC12 threshold is compared with the R12

342 value of samples in the test set. If RC12<R12, the prediction is considered a failure.

343 Prediction accuracy is calculated for each RC12 threshold, adjusting in 0.001 increments until

344 the highest prediction accuracy is achieved.

345 (5) Optimal RC12 threshold determination: The RC12 threshold with the highest

346 prediction accuracy is selected for each fold. The final RC12 threshold is determined by

347 averaging the optimal thresholds from all five folds.

348 **3.2.5 Spatial distribution of optimal threshold**

349 According to the optimal ratio coefficient threshold determined in section 3.2.4 and the

350 long-term and short-term rainfall parameters obtained through interpolation, the threshold

351 spatial distribution for the study area can be derived. Taking H12/D7 as an example, the

352 process is as follows:

353 First, by dividing the H12 values of each landslide point by the optimal ratio coefficient

354 RC12, the corresponding D7 thresholds for each landslide point can be calculated. These D7

355 thresholds serve as a basis for applying the Kriging interpolation method to obtain the spatial

356 distribution map of the D7 thresholds across the entire study area.

357 Next, by multiplying the D7 values of each landslide point by the ratio coefficient RC12,

358 the corresponding H12 thresholds for each landslide point can be determined. Subsequently,

359 utilizing these H12 thresholds, the Kriging interpolation method is applied once more to

360 generate the spatial distribution map of the H12 thresholds for the entire study area.

361 **3.3 Typhoon-specific rainfall-induced landslide warning system**

362 In order to effectively prevent typhoon-specific rainfall-induced landslide hazards,

363 constructing a comprehensive landslide warning system is crucial. This system integrates LSP

364 with critical rainfall thresholds, combining spatial probability and temporal probability to

365 predict the risk of landslide occurrence and the timing of potential events.

366 **3.3.1 Construction of the landslide warning system**

367   Using the natural breaks point method, the LSP is categorized into five levels of spatial

368   probability: very low (S1), low (S2), moderate (S3), high (S4), and very high (S5). These

369   levels represent varying degrees of susceptibility to landslides in different regions, forming

370   the basis for assessing landslide risks when combined with rainfall data. Paralleling the LSP

371   categorization, rainfall thresholds are also divided into five levels using the natural breaks

372   point method, representing temporal probability: very low (T1), low (T2), moderate (T3),

373   high (T4), and very high (T5). A lower rainfall threshold indicates a higher likelihood of

374   typhoon-induced landslides, thus signaling a greater risk of landslide events.

375   **Table 2** Classification of landslide hazard warning zones by integrating landslide susceptibility levels
376   (S1~S5) with rainfall threshold levels (T1~T5).

Landslide hazard warning zones	T1	T2	T3	T4	T5
S1 (very low)	No warning zone (2nd level)	No warning zone (1st level)	No warning zone (1st level)	No warning zone (1st level)	No warning zone (1st level)
S2 (low)	3rd level warning zone	No warning zone (2nd level)	No warning zone (2nd level)	No warning zone (1st level)	No warning zone (1st level)
S3 (moderate)	4th level warning zone	3rd level warning zone	3rd level warning zone	No warning zone (2nd level)	No warning zone (1st level)
S4 (high)	5th level warning zone	4th level warning zone	3rd level warning zone	No warning zone (2nd level)	No warning zone (1st level)
S5 (very high)	5th level warning zone	5th level warning zone	4th level warning zone	3rd level warning zone	No warning zone (2nd level)

377   The matrix-based integration of LSP results and rainfall thresholds, as presented in Table

378   2 (Segoni et al., 2015), highlights the correlation between landslide susceptibility and rainfall

379   intensity. As the levels of landslide hazard warnings escalate from the 1st level, indicating no

380   warning, to the 5th level, which signifies the highest alert, the likelihood of landslide

381   occurrences correspondingly increases. Areas categorized in higher hazard zones correspond

382   to regions with a heightened risk of landslides. This hazard warning system provides a spatial

383   framework for risk assessment and early warning, generating hazard zonation maps that can

384   be integrated into operational landslide monitoring and warning protocols. This underscores

385   the importance of implementing more effective geological disaster prevention strategies, as

386   thoroughly discussed in the literature by Huang et al. (2022).

4 Landslide susceptibility prediction using machine learning models

4.1 Statistical analysis of conditioning factors

The statistical analysis reveals distinct patterns of landslide susceptibility across all conditioning factors (Table S1 in the Supplement). Topographic factors demonstrate clear elevation-dependent behavior, with maximum susceptibility occurring at intermediate elevations (545-782 m, FR=1.637, IV=0.389), suggesting optimal conditions where weathering processes and slope instability converge. Slope gradient exhibits peak susceptibility in the moderate range (7.87–15.06°, FR=1.522, IV=0.343), indicating insufficient driving forces at gentler slopes and potential debris removal at steeper gradients. South-facing aspects show enhanced susceptibility (FR=1.299, IV=0.230), likely attributable to intensified weathering from solar radiation and moisture cycles.

Morphological indices reveal significant correlations with landslide occurrence. Profile curvature demonstrates highest susceptibility in convex areas (0.17–0.59, FR=1.480, IV=0.480), where stress concentration promotes slope failure. TWI shows strong positive correlation with wetness, peaking at high values (8.69–13.62, FR=1.799, IV=0.444), confirming the critical role of water accumulation in slope destabilization. SPI indicates maximum susceptibility in moderate stream power ranges (1.27–2.39, FR=1.298, IV=0.229), reflecting optimal erosional conditions.

Proximity factors exhibit contrasting patterns based on infrastructure type. Distance to roads shows strong inverse correlation with landslide occurrence (0–800 m, FR=1.499, IV=0.333), indicating anthropogenic disturbance effects. Conversely, distance to faults reveals a bimodal pattern with peak susceptibility at intermediate distances (7–12 km, FR=1.439, IV=0.305), suggesting regional structural influence rather than localized fault-induced instability. Environmental factors demonstrate vegetation's protective role, with moderate NDVI values (0.64–0.76) showing elevated susceptibility (FR=1.854, IV=0.015),

representing the transition zone between bare soil vulnerability and established vegetation stability. Lithological analysis reveals pronounced material control, with rhyolite (FR=1.546, IV=0.353) and granite (FR=1.247, IV=0.198) showing enhanced susceptibility due to intensive weathering and joint development, while sedimentary rocks (slate, shale, limestone, sandstone) exhibit strong resistance (FR<0.21) owing to their structural integrity and lower weathering susceptibility.

4.2 Landslide susceptibility modeling in Zixing City

Prior to model development, multicollinearity analysis was conducted using variance inflation factor (VIF) to ensure statistical reliability of the conditioning factors. The analysis revealed method-specific multicollinearity patterns: IV and CF methods showed no significant multicollinearity issues (all VIF < 10), while the FR method exhibited multicollinearity in four variables (SPI, Aspect, Plan curvature, and Distance to rivers with VIF > 10), which were subsequently excluded from FR-based modeling (Table S2 in the supplement). Following this preprocessing, landslide susceptibility prediction was performed using SVM and LightGBM models with the three distinct weighting methods (IV, CF, and FR). Susceptibility levels were categorized into five classes using the natural breaks classification method, with non-landslide samples strategically selected by excluding buffer zones of varying distances (0.1, 0.5, 1.0, 2.0, and 5.0 km) around documented landslide locations to optimize model performance and reduce spatial bias.

4.2.1 IV-based modeling performance

The IV-derived susceptibility maps (Fig. 4) revealed distinct spatial patterns between the two models across varying buffer distances. At smaller scales, the SVM model demonstrated more detailed classification, with a higher degree of overlap between high susceptibility areas and actual landslide locations. The LightGBM model's classification was smoother, with a lower degree of overlap between high susceptibility areas and actual landslide locations.

437 Notably, this performance discrepancy diminished progressively with increasing buffer

438 distances.
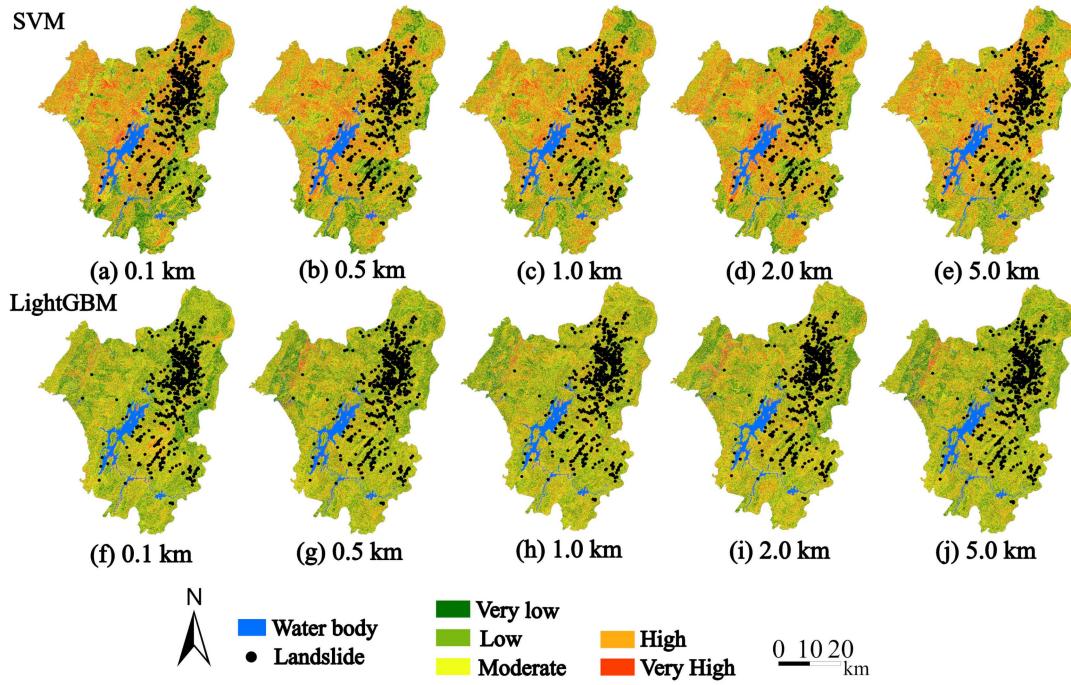
Figure 4 Landslide susceptibility map based on SVM and LightGBM models using the IV input.

4.2.2 CF-based modeling performance

442 In CF-based modeling (Fig. 5), the SVM model's high and very high landslide

443 susceptibility areas at smaller scales were more extensive than in the IV mode, with actual

444 landslide locations more frequently distributed within these high-risk areas. As the scale

445 increased, the high susceptibility areas gradually decreased. The LightGBM model also

446 showed a relatively smooth distribution, with some high susceptibility areas identified at

447 smaller scales gradually integrating as the scale increased, following a similar trend to the

448 SVM model.
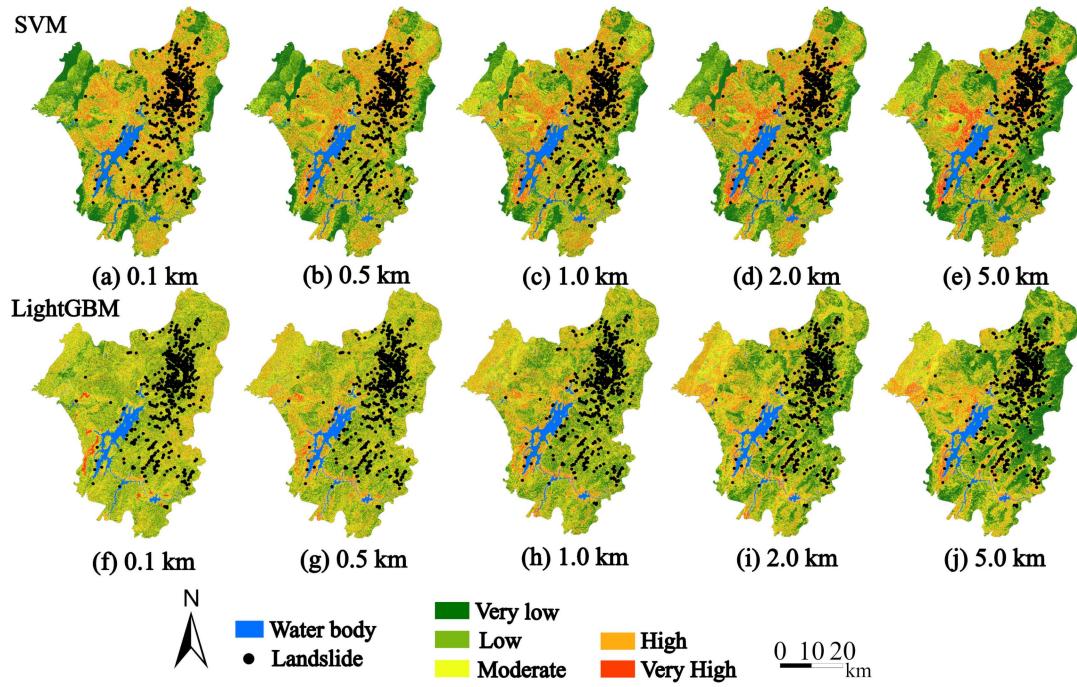
Figure 5 Landslide susceptibility map based on SVM and LightGBM models using the CF input.

4.2.3 FR-based modeling performance

Regarding the FR input (Fig. 6), the SVM model identified a significant number of high and very high landslide susceptibility areas at smaller scales compared to the IV and CF inputs, which closely matched the actual locations of landslides. As the buffer scale expanded, these high-risk areas generally diminished and the distribution became smoother. Conversely, the LightGBM model delivered more uniform results, offering broader moderate-risk distributions, with a small number of high susceptibility areas that did not align with the actual landslide locations. As the scale increased, the high susceptibility areas identified by the LightGBM model gradually diminished, showing greater consistency with the SVM model results at the higher scale.
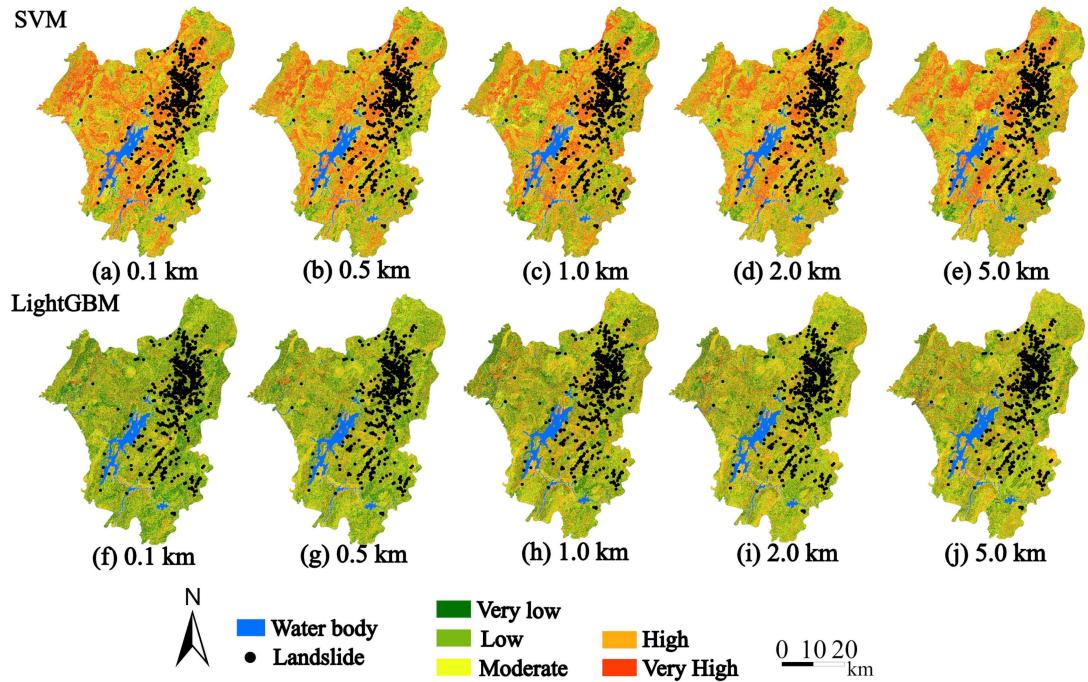
Figure 6 Landslide susceptibility map based on SVM and LightGBM models using the FR input.

4.3 Uncertainty analysis of LSP results

4.3.1 LSP accuracy evaluation and comparative performance

Table S2 (in the Supplement) demonstrates contrasting performance characteristics between the two machine learning approaches across different spatial scales and input configurations. LightGBM consistently achieved high AUC values (0.915–0.921) and maintained stable F1-scores (0.838–0.850) across all buffer distances and input methods, indicating robust generalization capability. In contrast, SVM exhibited pronounced sensitivity to parameter combinations, with performance varying significantly across different buffer distances (F1-scores ranging from 0.681 to 0.859) and input methods, particularly showing notable degradation with FR input at extreme spatial scales (0.1 km and 5.0 km).

Two configurations emerged as comprehensively superior: SVM with FR input at 0.5 km and 2.0 km buffer distances, both achieving F1-scores of 0.859. These optimal configurations not only maintained competitive AUC values (0.914 and 0.913 respectively) but demonstrated superior precision-recall balance compared to corresponding LightGBM configurations (F1-scores: 0.854 and 0.856). The high recall values (0.845 and 0.851) coupled with robust

478 precision (0.873 and 0.867) indicate enhanced sensitivity to landslide-prone areas while

479 minimizing false positive predictions. This bimodal performance pattern suggests that

480 intermediate buffer distances effectively capture fault-related geomorphological processes

481 influencing slope stability.

482 Independent validation on the test set confirmed the robustness of these optimal

483 configurations, with SVM-FR models at 0.5 km and 2.0 km buffer distances achieving F1-

484 scores of 0.847 and 0.852 respectively, representing minimal performance degradation from

485 training results. The consistent AUC values (0.909 and 0.908) on the test set further validate

486 the models' discriminative capability and indicate absence of overfitting, confirming the

487 reliability of these configurations for practical landslide susceptibility assessment applications.

488 **4.3.2   LSP distribution characteristics across conditions**

489 In addition to the performance metrics, the distribution characteristics of landslide

490 susceptibility predictions revealed fundamental differences between the models (Figs. S1–S3

491 in the Supplement). LightGBM generated smoother, more symmetrical distributions with

492 lower mean susceptibility values (0.196–0.320) and smaller standard deviations (0.099–

493 0.187), indicating stable and uniform predictions. In contrast, SVM exhibited greater

494 variability, with irregular distributions, higher mean values (0.303–0.515), and larger standard

495 deviations (0.112–0.214). Notably, SVM's mean susceptibility under FR input rose sharply

496 (0.446–0.515), while LightGBM maintained lower means despite moderately broader

497 deviations (0.160–0.187).

498 Therefore, SVM is preferable for FR-based modeling at 0.5 km and 2.0 km buffers,

499 where spatial precision is prioritized over prediction uniformity. The SVM model achieved its

500 highest accuracy at the 0.5 km buffer, classifying 86.4% of recorded landslides in high and

501 very high susceptibility zones (Fig. 6b). At the 2.0 km buffer (Fig. 6d), it still correctly

classified 82.1% of landslides in these zones. As a result, Fig. 6b is selected as the final landslide susceptibility map.

5 Landslide risk assessment in Zixing City

5.1 Critical rainfall thresholds for landslides in Zixing City

We evaluated four rainfall threshold models (H1-D7, H12-D7, H24-D7, and H72-D7) through 5-fold cross-validation, with their optimal ratio coefficient (RC) thresholds and prediction accuracies summarized in Table 3. The H24-D7 model, coupling 24-hour rainfall during landfall with 7-day antecedent moisture, achieved the highest accuracy (71.8%) by effectively capturing both cumulative saturation and abrupt triggering by typhoon rainfall bursts. Notably, the H24-D7 model exhibited stable performance across all folds, with accuracy ranging narrowly between 68.8% (Fold 1) and 74.6% (Fold 4), reflecting robust generalizability.

Table 3 Optimal RC values and prediction accuracies (%) for each model across 5-fold cross validation.

Model	Fold 1 RC/Accuracy	Fold 2 RC/Accuracy	Fold 3 RC/Accuracy	Fold 4 RC/Accuracy	Fold 5 RC/Accuracy	Average RC/Accuracy
H1-D7	0.032/56.5	0.062/29.7	0.076/35.5	0.022/53.6	0.040/47.8	0.047/44.6
H12-D7	0.077/54.2	0.167/46.6	0.243/48.3	0.267/47.7	0.154/45.3	0.182/48.5
H24-D7	0.472/68.8	0.436/72.3	0.422/73.1	0.459/74.6	0.414/70.2	**0.440/71.8**
H72-D7	0.789/56.5	0.776/59.4	0.781/63.1	0.802/51.4	0.783/60.1	0.787/58.1

In contrast, the H1-D7 and H12-D7 models displayed marked instability: H1-D7 accuracy fluctuated between 29.7% (Fold 2) and 56.5% (Fold 1), while H12-D7 thresholds (RC12: 0.077–0.267) corresponded to accuracies of 45.3–48.3%. The H72-D7 model showed moderate performance variability (accuracy: 51.4–63.1%) despite consistently high RC72 thresholds (>0.78).

These results highlight the critical role of temporal rainfall parameter selection. The superior performance of the H24-D7 model (24-hour short-term rainfall and 7-day antecedent rainfall) suggests that a 24-hour duration optimally captures both immediate landslide triggers

and cumulative hydrological effects, balancing sensitivity and stability. Shorter (H1/H12) or longer (H72) durations either overemphasize transient rainfall spikes or dilute critical triggering signals.

5.2 Spatio-temporal distribution of rainfall thresholds

Fig. 7 illustrates the spatial distribution of rainfall-triggered landslide thresholds derived from four models (RC1, RC12, RC24, and RC72) across multiple temporal scales (1-hour, 12-hour, 24-hour, 72-hour, and 7-day) within the study area.

5.2.1 Short-term predictions (1-hour to 12-hour scales)

At the 1-hour scale (Fig. 7a), the RC1 model generated thresholds ranging from 7 to 50 mm, with 65.2% of landslides occurring in moderate threshold zones (20–30 mm). This indicates the model's effectiveness in detecting slope failures under short-duration rainfall. In contrast, the RC12 model on the 12-hour scale (Fig. 7b) showed a wider threshold range (25–200 mm), with 62.9% of landslides in mid-to-high threshold regions (80–130 mm). This mismatch suggests that the 12-hour cumulative data may underestimate rainfall impacts in specific topographic settings.
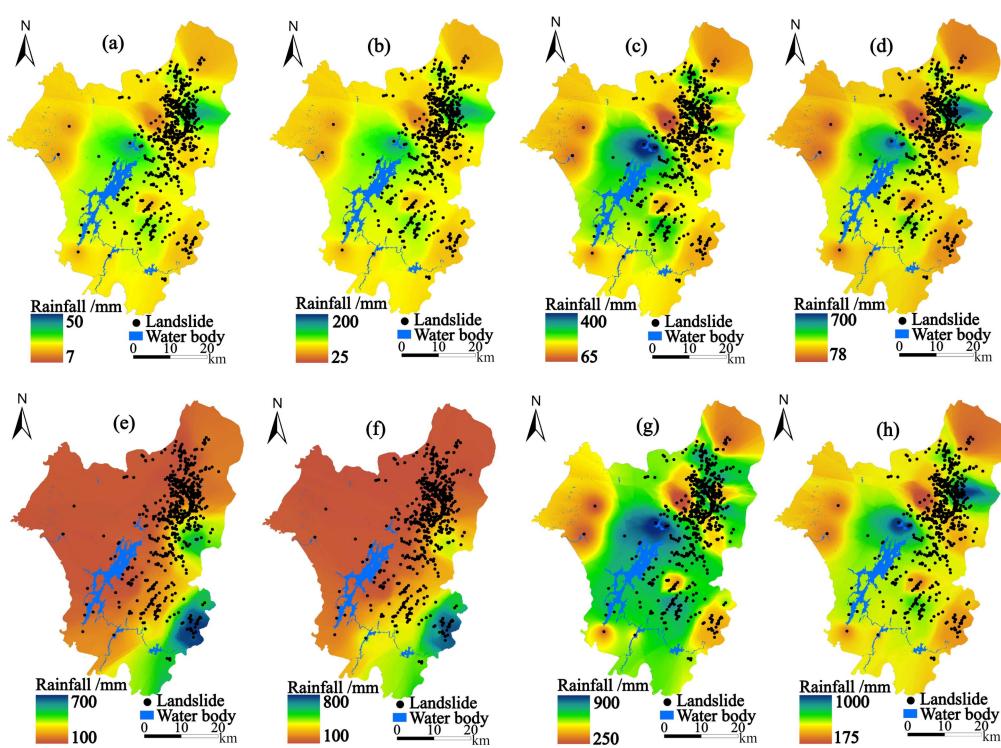
Figure 7 Distribution of typhoon rainfall thresholds under various optimal RC ratios: (a) 1-hour RC1-based, (b) 12-hour RC12-based, (c) 24-hour RC24-based, (d) 72-hour RC72-based, (e) 7-day RC1-based, (f) 7-day RC12-based, (g) 7-day RC24-based, and (h) 7-day RC72-based.

5.2.2 Mid-term predictions (24-hour to 72-hour scales)

The RC24 model at the 24-hour scale (Fig. 7c) displayed a threshold range of 65–400 mm, with 87.1% of landslides occurring within moderate thresholds (100–250 mm) and 12.3% in higher thresholds (>250 mm). This indicates a more accurate capture of rainfall intensity effects. At the 72-hour scale (Fig. 7d), the RC72 model produced thresholds between 78–700 mm, with 59.2% of landslides in mid-to-high threshold regions (200–500 mm). Although the RC72 model demonstrated reasonable sensitivity to prolonged rainfall, its upper threshold (700 mm) may result in conservative risk predictions for some geological settings.

5.2.3 Long-term predictions (7-day scale)

At the 7-day scale, significant differences emerge across models in terms of predicted rainfall thresholds and landslide points. The RC1 model (Fig. 7e) shows a threshold range of 100–700 mm, with landslide points predominantly concentrated in the lower rainfall ranges. While these low-threshold landslides may indicate localized risks, the model's conservative threshold distribution fails to effectively capture landslides triggered by higher rainfall amounts, potentially overlooking more significant events.

The RC12 model (Fig. 7f), with a threshold range of 100–800 mm, also shows a concentration of landslide points in the lower rainfall ranges. Despite a wider threshold range, the similarity to the RC1 model suggests that RC12 may also underutilize its capacity to predict higher typhoon-induced landslides, leading to under-prediction in areas experiencing moderate to heavy precipitation.

In contrast, the RC24 model (Fig. 7g) exhibits a balanced threshold range (250–900 mm) and effectively identifies landslide points in both moderate and high rainfall categories. This balance enables RC24 to capture the full spectrum of typhoon-induced landslides, accurately identifying risks across different rainfall intensities.

The RC72 model (Fig. 7h) shows a concentration of landslide points in the higher rainfall range (175–1000 mm). While it predicts landslides accurately under heavy rainfall conditions, the model may overestimate risks in some regions and neglect potential landslides associated with lower rainfall thresholds.

Based on the above analysis, the RC24 model is the optimal choice, which aligns with the findings in Section 5.1. Its effectiveness is evident as it demonstrates superior stability and accuracy in both the 24-hour and 7-day timescales.The RC24 model's balanced threshold range allows it to accurately assess landslide risks across varying rainfall intensities. This makes it the most reliable choice for practical landslide hazard warning applications.

5.3   Landslide hazard warning system for Zixing City

Based on the optimal LSP results (Fig. 6b) and the validated RC24 rainfall threshold model, a spatially explicit landslide hazard warning system was established for Zixing City. The integration of spatial probability (LSP) and temporal probability (rainfall thresholds) followed the matrix classification outlined in Table 2.

581
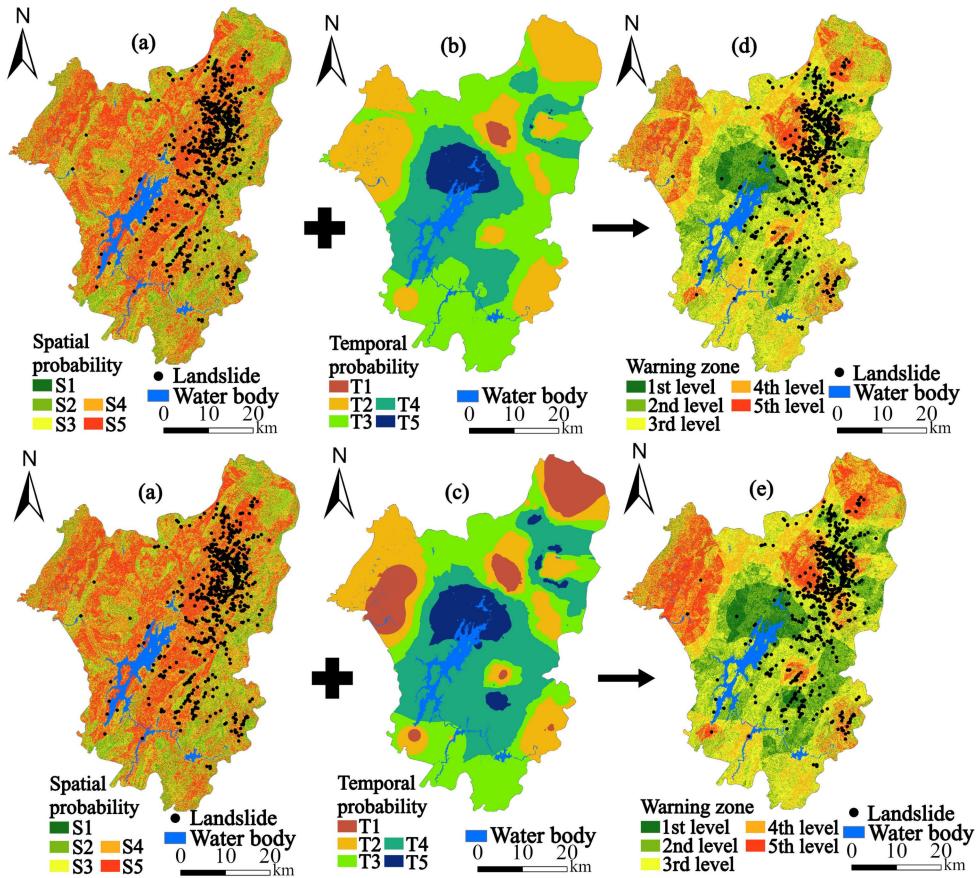
Figure 8 Landslide warning zones generated by overlaying spatial and temporal probability maps: (a) optimal spatial probability, (b) 24-hour RC24-based rainfall threshold, (c) 7-day RC24-based rainfall threshold, (d) overlay of (a) and (b), and (e) overlay of (a) and (c).

Five susceptibility levels in the LSP map (Fig. 6b) were replaced with five spatial probabilities (S1–S5) (Fig. 8a), respectively. Simultaneously, the spatially interpolated 24-hour rainfall thresholds (H24) (Fig. 8b) and 7-day effective rainfall thresholds (D7) (Fig. 8c) derived from the RC24 model were classified into five temporal probability levels (T1–T5) using the natural breaks method. Spatial overlay analysis was performed to combine the susceptibility levels (S1–S5) with the rainfall threshold levels (T1–T5), generating two hazard warning zone maps: H24-based (Fig. 8d) and D7-based (Fig. 8e).

Quantitative assessment of both warning systems reveals distinct performance characteristics. The 24-hour threshold system (Fig. 8d) demonstrates superior predictive efficiency, with 71.4% of historical landslides occurring within high to very high warning zones (Levels 3–5) while covering only 34.2% of the total area, resulting in an efficiency ratio

596 of 2.09 and a risk density of 49.0 landslides per 1000 high-risk grid cells. The spatial

597 distribution shows concentrated high-risk areas primarily in the central region, characterized

598 by steep slopes (>21.80°), weathered granite lithology, and road proximity (0–800 m). This

599 focused distribution indicates effective identification of areas most sensitive to short-term

600 intense rainfall triggers.

601 The 7-day threshold system (Fig. 8e) exhibits broader spatial coverage, with high-risk

602 zones encompassing 42.7% of the study area and capturing 68.7% of historical landslides,

603 yielding a lower efficiency ratio of 1.61 and risk density of 37.8 landslides per 1000 grid cells.

604 This system effectively identifies extended vulnerable areas in northern and eastern regions,

605 reflecting cumulative rainfall effects on slope stability. The expanded coverage captures zones

606 where prolonged antecedent moisture interacts with moderate-to-high susceptibility

607 conditions.

608 Statistical validation confirms the complementary nature of both systems. The 24-hour

609 system achieves higher spatial efficiency (efficiency ratio 2.09 vs. 1.61) and landslide

610 concentration (risk density 49.0 vs. 37.8), making it optimal for immediate typhoon response

611 and targeted emergency resource allocation. Conversely, the 7-day system provides

612 comprehensive coverage for prolonged rainfall scenarios, essential for early warning during

613 extended typhoon events despite its broader spatial distribution and lower concentration

614 efficiency. The combined application of both systems enables dynamic hazard assessment,

615 addressing both rapid-onset failures during typhoon landfall and delayed failures following

616 sustained precipitation.

617 **6 Discussion**

618 **6.1 Model selection strategy and optimization of LSP**

619

620   Our comparative analysis of SVM and LightGBM across different input methods (IV,

621 CF, FR) and buffer distances shows distinct performance patterns crucial for model selection

622 in typhoon-induced LSP. SVM exhibited marked sensitivity to configuration parameters, with

623 F1-scores varying from 0.681 to 0.859 depending on buffer distance and input method.

624 LightGBM maintained more stable performance (F1-scores: 0.838–0.850) across all

625 configurations. These differences reflect fundamental algorithmic characteristics: SVM's

626 kernel-based approach effectively captures localized patterns when properly tuned, while

627 LightGBM's ensemble structure delivers consistent results across varying data conditions.

628   SVM's superior performance at 0.5–2.0 km buffer distances with FR weighting builds on

629 findings by Kalantar et al. (2018) and Bogaard and Greco (2018). This buffer range appears

630 effective for capturing the spatial patterns of typhoon-induced failures in our study area. FR

631 weighting's effectiveness supports Reichenbach et al. (2018) and Yan et al. (2019), who found

632 that frequency-based methods excel at quantifying terrain-landslide relationships. In typhoon

633 conditions, FR effectively weights critical factors including road proximity and weathered

634 granite lithology.

635   These performance patterns justify our dual-model approach. SVM, though requiring

636 careful calibration, enables precise delineation of high-risk zones essential for emergency

637 response, with SVM-FR at 0.5 km achieving peak accuracy (F1=0.859). LightGBM's

638 robustness suits operational contexts requiring consistent predictions under variable

639 conditions. Our results suggest that effective model selection depends on matching

640 algorithmic strengths to specific application requirements rather than identifying a universally

641 superior algorithm.

642 **6.2 Rainfall threshold modeling and typhoon-specific mechanisms**

643

The H24-D7 model achieved 71.8% accuracy, outperforming alternative temporal windows (Table 3). The optimal RC24 value of 0.440 (with inter-fold variation of 0.414–0.472) indicates that landslides typically occur when 24-hour rainfall constitutes approximately 44% of the preceding 7-day accumulation. This pattern is consistent with the multi-temporal triggering framework proposed by Nolasco-Javier and Kumar (2018) for typhoon contexts, where both antecedent saturation and short-term intensity contribute to slope failure. However, the specific hydrological mechanisms underlying this ratio require verification through in-situ soil moisture monitoring. The H1-D7 and H12-D7 models showed lower and more variable accuracy (44.6% and 48.5% respectively), suggesting that shorter accumulation periods may inadequately represent the cumulative soil saturation process relevant to this region's geological conditions (Kirschbaum and Stanley, 2018).

Spatial patterns in rainfall thresholds reveal systematic variations across the study area. Southeastern regions exhibit elevated H24 thresholds exceeding 250 mm (Fig. 7c), while northern areas show reduced thresholds of 100–150 mm. These spatial variations align with findings by Lee et al. (2018) and Cho et al. (2022) regarding topographic controls on typhoon-induced landslides, though the specific mechanisms require further investigation with detailed meteorological analysis. The spatially distributed thresholds derived through Kriging interpolation (Table 1) provide location-specific values that improve upon uniform regional thresholds typically employed in operational systems (Segoni et al., 2018b).

The consistent performance across the five validation folds (68.8–74.6% accuracy) demonstrates the model's stability when applied to different spatial subsets of the landslide inventory. This suggests the H24-D7 relationship captures generalizable rainfall-slope response patterns rather than site-specific anomalies, though validation with independent typhoon events would further confirm model robustness.

6.3 Integration of susceptibility and rainfall thresholds for landslide warning

669   The integrated warning system combines static susceptibility surfaces with spatially

670   continuous rainfall thresholds following the matrix framework in Table 2. The H24-based

671   system (Fig. 8d) captured 71.4% of historical landslides within high to very high warning

672   zones (Levels 3–5) covering 34.2% of the study area, yielding an efficiency ratio of 2.09. The

673   D7-based system (Fig. 8e) identified 68.7% of landslides across 42.7% of the area (efficiency

674   ratio: 1.61). These focused distributions contrast with the broader spatial coverage typically

675   required by uniform regional thresholds (Guzzetti et al., 2020), though direct comparative

676   validation would be needed to quantify the performance gain.

677   The dual-threshold configuration provides complementary perspectives suited to

678   different phases of typhoon evolution, with D7 reflecting cumulative moisture conditions and

679   H24 capturing immediate triggering rainfall. This combination addresses the compound

680   rainfall mechanisms documented in typhoon-affected regions (Gariano et al., 2015; Nolasco-

681   Javier and Kumar, 2018), though the optimal application strategy for operational warning

682   would require integration with real-time meteorological forecasting systems.

683   Spatially continuous thresholds (Fig. 8b, c) address terrain-induced variability more

684   effectively than point-based approaches. The Kriging interpolation method provides threshold

685   estimates across the entire study area, accounting for spatial autocorrelation in rainfall

686   patterns (Table 1). However, threshold accuracy depends on rain gauge density and may

687   decline in areas distant from monitoring stations, as indicated by the interpolation validation

688   metrics (R: 0.76–0.87, NSE: 0.71–0.82). The framework advances beyond existing point-

689   based threshold systems (Segoni et al., 2018b; Guzzetti et al., 2020) by providing spatially

690   explicit hazard assessment, though regional adaptation of threshold parameters would be

691   necessary for application in different geological settings.

692   The modular design allows the framework to be adapted for operational landslide early

693   warning, though practical implementation would require integration with meteorological

monitoring infrastructure, standardized protocols for warning dissemination, and post-event validation procedures to maintain system reliability. These operational considerations extend beyond the methodological scope of this study but represent important directions for future development of typhoon-specific landslide warning systems.

6.4 Limitations and future research directions

Despite promising advancements, this study has limitations owing to the complexity of typhoon-induced landslides. First, the model's validation relies solely on landslides from Typhoon Gaemi. While this single event provided a comprehensive dataset, validating against multiple, varied typhoons is crucial for model robustness. Typhoons differ significantly in intensity, rainfall patterns, forward speed, and seasonality, all of which can influence threshold parameters. For instance, a slow-moving typhoon with higher cumulative rainfall and lower peak intensity could alter the optimal H24-D7 ratios. Future research should incorporate landslide inventories from typhoons with contrasting characteristics to assess threshold transferability and develop adaptive parameterization. The framework's modular design readily facilitates this by allowing recalibration of the RC24 coefficient for different typhoon types.

Second, the current study primarily addresses rainfall-induced landslides, overlooking other potential contributing factors. Future work should explore integrating multiple triggering mechanisms, including earthquakes, human-induced slope modifications, and typhoon rainfall, for a more comprehensive hazard assessment.

Third, the study doesn't explicitly address the potential impacts of climate change on typhoon rainfall and landslide occurrence. As climate change alters typhoon frequency, intensity, and tracks, future studies should incorporate climate projections specific to typhoon-prone regions. This will enable the development of forward-looking landslide warning systems that can adapt to the evolving threats posed by typhoon-specific rainfall.

Fourth, while this study demonstrates the effectiveness of ML approaches, further refinement is possible. Future research should explore advanced deep learning techniques and ensemble methods to better capture the complex, non-linear relationships between typhoon-related variables (e.g., rainfall intensity, duration, antecedent moisture) and slope stability. These advanced methods may offer improved predictive accuracy, more robust uncertainty quantification, and ultimately, more reliable hazard warnings.

Finally, climate projections for Southeast China show a 15–25% increase in peak typhoon rainfall by 2080 (RCP8.5), which could alter the H24–D7 landslide thresholds from this study. Higher atmospheric moisture may lower D7 thresholds, while greater rainfall intensity could require new H24 parameters. Shifting typhoon tracks and seasonality might also change which areas are vulnerable. Future work must use downscaled climate data to create non-stationary thresholds, ensuring the long-term reliability of warning systems in the region.

7 Conclusions

This study establishes a novel integrated framework combining optimized LSP with typhoon-specific rainfall threshold modeling for comprehensive hazard assessment in mountainous regions. Through systematic analysis of 705 landslides triggered by Typhoon Gaemi in Zixing City, several key insights emerge:

(1) Buffer distance optimization proves critical for typhoon-induced landslide modeling, with SVM-FR combinations at 0.5–2.0 km distances achieving superior performance (F1-score: 0.859) compared to conventional approaches. This spatial scale effectively captures typhoon-induced moisture infiltration patterns that differ fundamentally from other triggering mechanisms.

(2) The H24-D7 threshold model demonstrates exceptional stability (71.8% accuracy across 5-fold validation), successfully characterizing the dual-phase failure mechanism unique

to typhoons: prolonged antecedent saturation coupled with intense precipitation bursts during typhoon passage.

(3) Spatially distributed rainfall thresholds reveal significant heterogeneity, reflecting complex interactions between typhoon structure and local topography that contradict uniform regional threshold assumptions in existing operational systems.

(4) The integrated warning system achieves operational efficiency through dual-threshold configuration: H24 thresholds provide immediate response capability during typhoon landfall, while D7 thresholds enable early detection of vulnerable areas approaching saturation conditions.

(5) This framework addresses three critical gaps in current landslide prediction: systematic buffer optimization for imbalanced datasets, effective integration of variable weighting with machine learning algorithms, and development of typhoon-specific spatially explicit thresholds.

Code and data availability. The source code and data will be made available on request.

Competing interests. The contact author has declared that none of the authors has any competing interests.

Author contributions. **Weifeng Xiao**: Writing-review & editing, Validation, Conceptualization. **Guangchong Yao**: Visualization, Validation, Data curation. **Zhenghui Xiao**: Writing-review & editing, Formal analysis. **Ge Liu**: Correspondence, Funding acquisition. **Luguang Luo**: Visualization, Validation, Investigation, Data curation. **Yunjiang Cao**: Visualization, Formal analysis, Data curation. **Wei Yin**: Validation, Investigation.

Acknowledgments. This research was jointly funded by the National Key Research and Development Program of China (2024YFD1500602), the Research Project on Natural

770 Resources of Hunan Provincial Department of Natural Resources (No. HBZ20240112), and

771 the National Natural Science Foundation of China (No. 42171385, U2243230).

772

773

774

775

References

777 Achu, A. L., Aju, C. D., Pham, Q. B., Reghunath, R., and Anh, D. T.: Landslide susceptibility modeling

778   using hybrid bivariate statistical - based machine - learning method in a highland segment of Southern

779   Western Ghats, India, Environ. Earth Sci., 81, 361, https://doi.org/10.1007/s12665-022-10464-z, 2022.

780 Banfi, F. and De Michele, C.: Temporal clustering of precipitation driving landslides over the Italian

781   Territory, Earths Future, 12, e2023EF003885, https://doi.org/10.1029/2023EF003885, 2024.

782 Bogaard, T. and Greco, R.: Hydrological perspectives on precipitation intensity-duration thresholds for

783   landslide initiation: proposing hydro-meteorological thresholds, Nat. Hazards Earth Syst. Sci., 18, 31–39,

784   https://doi.org/10.5194/nhess-18-31-2018, 2018.

785 Calvello, M. and Piciullo, L.: Assessing the performance of regional landslide early warning models: the

786   EDuMaP method, Nat. Hazards Earth Syst. Sci., 16, 103–122, https://doi.org/10.5194/nhess-16-103-

787   2016, 2016.

788 Chang, Z. L., Huang, J. S., Huang, F. M., Bhuyan, K., Meena, S. R., and Catani, F.: Uncertainty analysis of

789   non-landslide sample selection in landslide susceptibility prediction using slope unit-based machine

790   learning models, Gondwana Res., 117, 307–320, https://doi.org/10.1016/j.gr.2023.02.007, 2023.

791 Cho, W., Park, J., Moon, J., Cha, D. H., Moon, Y. M., Kim, H. S., Noh, K. J., and Park, S. H.: Effects of

792   topography and sea surface temperature anomalies on heavy rainfall induced by Typhoon Chaba in 2016,

793   Geosci. Lett., 9, 29, https://doi.org/10.1186/s40562-022-00230-1, 2022.

794 Chung, C. C. and Li, Z. Y.: Rapid landslide risk zoning toward multi-slope units of the Neikuihui tribe for

795   preliminary disaster management, Nat. Hazards Earth Syst. Sci., 22, 1777–1794,

796   https://doi.org/10.5194/nhess-22-1777-2022, 2022.

Ciurleo, M., Cascini, L., and Calvello, M.: A comparison of statistical and deterministic methods for shallow landslide susceptibility zoning in clayey soils, Eng. Geol., 223, 71–81, https://doi.org/10.1016/j.enggeo.2017.04.023, 2017.

Dou, H. Q., He, J. B., Huang, S. Y., Jian, W. B., and Guo, C. X.: Influences of non - landslide sample selection strategies on landslide susceptibility mapping by machine learning, Geomat. Nat. Haz. Risk, 14, 1–15, https://doi.org/10.1080/19475705.2023.2285719, 2023.

Fan, W., Wei, Y. N., and Deng, L. S.: Failure modes and mechanisms of shallow debris landslides using an artificial rainfall model experiment on Qin-ba Mountain, Int. J. Geomech., 18, 04017157, https://doi.org/10.1061/(ASCE)GM.1943 - 5622.0001068, 2018.

Fan, X. M., Scaringi, G., Korup, O., West, A. J., van Westen, C. J., Tanyas, H., Hovius, N., Hales, T. C., Jibson, R. W., Allstadt, K. E., Zhang, L. M., Evans, S. G., Xu, C., Li, G., Pei, X. J., Xu, Q., & Huang, R. Q. (2019). Earthquake-Induced Chains of Geologic Hazards: Patterns, Mechanisms, and Impacts. Reviews of Geophysics, 57(2), 421-503. https://doi.org/10.1029/2018RG000626.

Froude, M. J., and Petley, D. N.: Global fatal landslide occurrence from 2004 to 2016, Nat. Hazards Earth Syst. Sci., 18, 2161–2181, https://doi.org/10.5194/nhess - 18 - 2161 - 2018, 2018.

Gariano, S. L., Brunetti, M. T., Iovine, G., Melillo, M., Peruccacci, S., Terranova, O., Vennari, C., and Guzzetti, F.: Calibration and validation of rainfall thresholds for shallow landslide forecasting in Sicily, southern Italy, Geomorphology, 228, 653–665, https://doi.org/10.1016/j.geomorph.2014.10.019, 2015.

Gariano, S. L., and Guzzetti, F.: Landslides in a changing climate, Earth - Sci. Rev., 162, 227–252, https://doi.org/10.1016/j.earscirev.2016.08.011, 2016.

Guo, W. X., Ye, J., Liu, C. B., Lv, Y. J., Zeng, Q. Y., and Huang, X.: An approach for predicting landslide susceptibility and evaluating predisposing factors, Int. J. Appl. Earth Obs., 135, 104217, https://doi.org/10.1016/j.jag.2024.104217, 2024.

Guzzetti, F., Gariano, S. L., Peruccacci, S., Brunetti, M. T., Marchesini, I., Rossi, M., and Melillo, M.: Geographical landslide early warning systems, Earth - Sci. Rev., 200, 102973, https://doi.org/10.1016/j.earscirev.2019.102973, 2020.

Guzzetti, F.: Invited perspectives: Landslide populations - can they be predicted?, Nat. Hazards Earth Syst. Sci., 21, 1467–1471, https://doi.org/10.5194/nhess - 21 - 1467 - 2021, 2021.

825 Huang, F., Chen, J., Liu, W., Huang, J., Hong, H., and Chen, W.: Regional rainfall - induced landslide

826   hazard warning based on landslide susceptibility mapping and a critical rainfall threshold,

827   Geomorphology, 408, 108236, https://doi.org/10.1016/j.geomorph.2022.108236, 2022.

828 Huang, Y., and Zhao, L.: Review on landslide susceptibility mapping using support vector machines,

829   Catena, 165, 520–529, https://doi.org/10.1016/j.catena.2018.03.003, 2018.

830 Kalantar, B., Pradhan, B., Naghibi, S. A., Motevalli, A., and Mansor, S.: Assessment of the effects of

831   training data selection on the landslide susceptibility mapping: A comparison between support vector

832   machine (SVM), logistic regression (LR), and artificial neural networks (ANN), Geomat. Nat. Haz. Risk,

833   9, 49–69, https://doi.org/10.1080/19475705.2017.1407368, 2018.

834 Kenanoglu, M. B., Ahmadi - Adli, M., Toker, N. K., and Huvaj, N.: Effect of unsaturated soil properties on

835   the intensity-duration threshold for rainfall triggered landslides, Tek. Dergi, 30, 9009–9027,

836   https://doi.org/10.18400/tekderg.414884, 2019.

837 Kirschbaum, D. and Stanley, T.: Satellite-Based Assessment of Rainfall-Triggered Landslide Hazard for

838   Situational Awareness, Earths Future, 6, 505–523, https://doi.org/10.1002/2017EF000715, 2018.

839 Lee, J. T., Ko, K. Y., Lee, D. I., You, C. H., and Liou, Y. C.: Enhancement of orographic precipitation in

840   Jeju Island during the passage of Typhoon Khanun (2012), Atmos. Res., 201, 58–71,

841   https://doi.org/10.1016/j.atmosres.2017.10.013, 2018.

842 Li, Y. L., Lin, Y. L., and Wang, Y. Q.: A numerical study on the formation and maintenance of a long -

843   lived rainband in Typhoon Longwang (2005), J. Geophys. Res. Atmos., 124(19), 10401–10426,

844   https://doi.org/10.1029/2019JD030600, 2019.

845 Liu, L. L., Zhang, Y. L., Xiao, T., and Yang, C.: A frequency ratio - based sampling strategy for landslide

846   susceptibility assessment, Bull. Eng. Geol. Environ., 81, 360, https://doi.org/10.1007/s10064 - 022 -

847   02836 - 3, 2022.

848 Lombardo, L., and Mai, P. M.: Presenting logistic regression - based landslide susceptibility results, Eng.

849   Geol., 244, 14–24, https://doi.org/10.1016/j.enggeo.2018.07.019, 2018.

850 Ma, H., Wang, F. W., Fu, Z. J., Feng, Y. Q., You, Q., and Li, S.: Characterizing the clustered landslides

851   triggered by extreme rainfall during the 2024 typhoon Gaemi in Zixing City, Hunan Province, China,

852   Landslides, 22, 2311–2329, https://doi.org/10.1007/s10346-025-02510-1, 2025.

853 Merghadi, A., Yunus, A. P., Dou, J., Whiteley, J., ThaiPham, B., Bui, D. T., Avtar, R., and Abderrahmane,

854   B.: Machine learning methods for landslide susceptibility studies: A comparative overview of algorithm

855   performance, Earth-Sci. Rev., 207, 103225, https://doi.org/10.1016/j.earscirev.2020.103225, 2020.

856 Mirus, B. B., Becker, R. E., Baum, R. L., and Smith, J. B.: Integrating real-time subsurface hydrologic

857   monitoring with empirical rainfall thresholds to improve landslide early warning, Landslides, 15, 1909–

858   1919, https://doi.org/10.1007/s10346-018-0995-z, 2018.

859 Mondini, A. C., Guzzetti, F., and Melillo, M.: Deep learning forecast of rainfall-induced shallow landslides,

860   Nat. Commun., 14, 10.1038/s41467-023-38135-y, https://doi.org/10.1038/s41467-023-38135-y, 2023.

861 Niu, H. T., Shao, S. J., Gao, J. Q., and Jing, H.: Research on GIS-based information value model for

862   landslide geological hazards prediction in soil - rock contact zone in southern Shaanxi, Phys. Chem.

863   Earth, 133, 103515, https://doi.org/10.1016/j.pce.2023.103515, 2024.

864 Nocentini, N., Medici, C., Barbadori, F., Gatto, A., Franceschini, R., del Soldato, M., Rosi, A., and Segoni,

865   S.: Optimization of rainfall thresholds for landslide early warning through false alarm reduction and a

866   multi-source validation, Landslides, 21, 557–571, https://doi.org/10.1007/s10346-023-02176-7, 2024.

867 Nolasco-Javier, D. and Kumar, L.: Deriving the rainfall threshold for shallow landslide early warning

868   during tropical cyclones: a case study in northern Philippines, Nat. Hazards, 90, 921–941,

869   https://doi.org/10.1007/s11069-017-3081-2, 2018.

870 Panchal, S., and Shrivastava, A. K.: A comparative study of frequency ratio, Shannon's entropy and

871   analytic hierarchy process (AHP) models for landslide susceptibility assessment, ISPRS Int. J. Geo-Inf.,

872   10, 603, https://doi.org/10.3390/ijgi10090603, 2021.

873 Piciullo, L., Calvello, M., and Cepeda, J. M.: Territorial early warning systems for rainfall - induced

874   landslides, Earth-Sci. Rev., 179, 228–247, https://doi.org/10.1016/j.earscirev.2018.02.013, 2018.

875 Piciullo, L., Gariano, S. L., Melillo, M., Brunetti, M. T., Peruccacci, S., Guzzetti, F., and Calvello, M.:

876   Definition and performance of a threshold - based regional early warning model for rainfall - induced

877   landslides, Landslides, 14, 995–1008, https://doi.org/10.1007/s10346-016-0750-2, 2017.

878 Regmi, N. R., Walter, J. I., Jiang, J. L., Orban, A. M., and Hayman, N. W.: Spatial patterns of landslides in

879   a modest topography of the Ozark and Ouachita Mountains, USA, Catena, 245, 108344,

880   https://doi.org/10.1016/j.catena.2024.108344, 2024.

881 Reichenbach, P., Rossi, M., Malamud, B. D., Mihir, M., and Guzzetti, F.: A review of statistically - based

882 landslide susceptibility models, Earth-Sci. Rev., 180, 60–91,

883 https://doi.org/10.1016/j.earscirev.2018.03.001, 2018.

884 Sahin, E. K.: Comparative analysis of gradient boosting algorithms for landslide susceptibility mapping,

885 Geocarto Int., 37, 2441–2465, https://doi.org/10.1080/10106049.2020.1831623, 2022.

886 San, B. T.: An evaluation of SVM using polygon-based random sampling in landslide susceptibility

887 mapping: The Candir catchment area (western Antalya, Turkey), Int. J. Appl. Earth Obs., 26, 399–412,

888 https://doi.org/10.1016/j.jag.2013.09.010, 2014.

889 Segoni, S., Lagomarsino, D., Fanti, R., Moretti, S., and Casagli, N.: Integration of rainfall thresholds and

890 susceptibility maps in the Emilia Romagna (Italy) regional - scale landslide warning system, Landslides,

891 12, 773–785, https://doi.org/10.1007/s10346-014-0502-0, 2015.

892 Segoni, S., Piciullo, L., and Gariano, S. L.: A review of the recent literature on rainfall thresholds for

893 landslide occurrence, Landslides, 15, 1483–1501, https://doi.org/10.1007/s10346-018-0966-4, 2018a.

894 Segoni, S., Rosi, A., Lagomarsino, D., Fanti, R., and Casagli, N.: Brief communication: Using averaged

895 soil moisture estimates to improve the performances of a regional - scale landslide early warning system,

896 Nat. Hazards Earth Syst. Sci., 18, 807–812, https://doi.org/10.5194/nhess-18-807-2018, 2018b.

897 Steger, S., Brenning, A., Bell, R., and Glade, T.: The propagation of inventory - based positional errors into

898 statistical landslide susceptibility models, Nat. Hazards Earth Syst. Sci., 16, 2729–2745,

899 https://doi.org/10.5194/nhess-16-2729-2016, 2016.

900 Sun, D. L., Wu, X. Q., Wen, H. J., and Gu, Q. Y.: A LightGBM-based landslide susceptibility model

901 considering the uncertainty of non-landslide samples, Geomat. Nat. Haz. Risk, 14, 2213807,

902 https://doi.org/10.1080/19475705.2023.2213807, 2023.

903 Sun, Y., Zhang, J., Wang, H. A., and Lu, D. G.: Probabilistic thresholds for regional rainfall induced

904 landslides, Comput. Geotech., 166, 106040, https://doi.org/10.1016/j.compgeo.2023.106040, 2024.

905 Thiene, M., Shaw, W. D., and Scarpa, R.: Perceived risks of mountain landslides in Italy: Stated choices for

906 subjective risk reductions, Landslides, 14, 1077–1089, https://doi.org/10.1007/s10346-016-0741-3, 2017.

907 Tufano, R., Formetta, G., Calcaterra, D., and De Vita, P.: Hydrological control of soil thickness spatial

908 variability on the initiation of rainfall-induced shallow landslides using a three - dimensional model,

909 Landslides, 18, 3367–3380, https://doi.org/10.1007/s10346-021-01681 - x, 2021.

910   Xiao, W. F., Zhou, Z. Y., Ren, B. Z., and Deng, X. P.: Integrating spatial clustering and multi - source

911   geospatial data for comprehensive geological hazard modeling in Hunan Province, Sci. Rep., 15, 1982,

912   https://doi.org/10.1038/s41598-024-84825 - y, 2025.

913   Yan, F., Zhang, Q. W., Ye, S., and Ren, B.: A novel hybrid approach for landslide susceptibility mapping

914   integrating analytical hierarchy process and normalized frequency ratio methods with the cloud model,

915   Geomorphology, 327, 170–187, https://doi.org/10.1016/j.geomorph.2018.10.024, 2019.

916   Yang, C., Liu, L. L., Huang, F. M., Huang, L., and Wang, X. M.: Machine learning - based landslide

917   susceptibility assessment with optimized ratio of landslide to non-landslide samples, Gondwana Res.,

918   123, 198–216, https://doi.org/10.1016/j.gr.2022.05.012, 2023.

919   Yang, K. H., Uzuoka, R., Thuo, J. N., Lin, G. L., and Nakai, Y.: Coupled hydro-mechanical analysis of two

920   unstable unsaturated slopes subject to rainfall infiltration, Eng. Geol., 216, 13–30,

921   https://doi.org/10.1016/j.enggeo.2016.11.006, 2017.

922   Zêzere, J. L., Pereira, S., Melo, R., Oliveira, S. C., and Garcia, R. A. C.: Mapping landslide susceptibility

923   using data-driven methods, Sci. Total Environ., 589, 250–267,

924   https://doi.org/10.1016/j.scitotenv.2017.02.188, 2017.

925   Zhao, Z., Liu, Z. Y., and Xu, C.: Slope unit-based landslide susceptibility mapping using certainty factor,

926   support vector machine, random forest, CF-SVM and CF-RF models, Front. Earth Sci., 9, 589630,

927   https://doi.org/10.3389/feart.2021.589630, 2021.

928   Zou, Y., Wei, Z. F., Zhan, Q. M., and Zhou, H. J.: An extreme storm over the Nanling Mountains during

929   Typhoon Bilis and the roles of terrain, Nat. Hazards, 116, 795–815, https://doi.org/10.1007/s11069-022-

930   05699-9, 2023.